RSC Advances

PAPER

View Article Online
View Journal | View Issue

Cite this: *RSC Adv.*, 2018, **8**, 29871

Composition design, electrical properties, and temperature stability in (1 − *x*) $K_{0.44}Na_{0.56}Nb_{0.96}Sb_{0.04}O_3$-$xBi_{0.45}La_{0.05}Na_{0.5}ZrO_3$ lead-free ceramics

Jian Ma,*[a] Juan Wu[a] and Bo Wu *[b]

Received 21st July 2018
Accepted 17th August 2018

DOI: 10.1039/c8ra06183a

rsc.li/rsc-advances

In this work, we designed a new system of $(1-x)K_{0.44}Na_{0.56}Nb_{0.96}Sb_{0.04}O_3$-$xBi_{0.45}La_{0.05}Na_{0.5}ZrO_3$ (KNNS-*x*BLNZ, $0 \leq x \leq 0.06$) ceramics, and systemically investigated both their electrical performance and temperature stability. Through optimizing the composition, a relatively good comprehensive performance (*e.g.*, $d_{33} \sim 455 \pm 10$ pC N^{-1}, $k_p \sim 0.47 \pm 0.02$, $T_C \sim 266$ °C, strain ∼ 0.148%, and $d_{33}^* \sim 493$ pm V^{-1}) is obtained in the ceramics with $x = 0.040$, which is attributed to the construction of a rhombohedral–orthorhombic–tetragonal (R–O–T) phase boundary. Moreover, a good temperature stability of remnant polarization (P_r) as well as strain value ($P_{r100\ °C}/P_{rRT} \sim 89.6\%$, $P_{r180\ °C}/P_{rRT} \sim 73.2\%$, $S_{100\ °C}/S_{RT} \sim 92.6\%$, $S_{180\ °C}/S_{RT} \sim 74.1\%$) is gained in KNNS-0.040BLNZ ceramics with a broad temperature range from room temperature to 180 °C. Hence, we believe that KNNS-*x*BLNZ ceramics opens a window for the practical application of lead-free ceramics.

1. Introduction

Piezoelectric materials play an important role in electronic devices because they can interconvert electrical energy into mechanical energy. Lead zirconate titanate ($PbZr_{1-x}Ti_xO_3$, PZT) ceramics have been the dominating material in the piezoelectric market during the last 60 years.[1] However, in order to protect the environment and human sustainable development due to the toxicity of lead in the compositions, a lot of effort has been recently devoted to develop high-performance lead-free piezoelectric ceramics which can eventually replace the lead-based ones.[1–26]

Among all the lead-free piezoelectric materials, (K, Na)NbO_3 has been regarded as a potential candidate due to its good comprehensive electrical properties especially its flexibility in terms of compositional modification.[2–26] Saito *et al.* reported that alkali niobate ceramics based on Li, Ta, and Sb-modified KNN show high density and excellent performance ($d_{33} \sim 416$ pC N^{-1}; $T_C \sim 253$ °C) by the reactive-templated grain growth method in 2004.[2] Ever then, researchers paid much attention to promote the electricity by constructing the multiphase boundary has been extensively applied in KNN-based lead-free materials.[2–26] Recently, some breakthroughs in the KNN-based ceramics were achieved.[4–7,32–34] For example, Wu *et al.* obtained a series of KNN-based lead-free ceramics systems in multiphase boundary (*e.g.*, R–O–T, R–T) with giant piezoelectricity of ≥490 pC N^{-1}, which are comparable to that of PZT materials.[4–7] According to the previous works, Sb^{5+}, $Bi_{0.5}M_{0.5}ZrO_3$ (M = Na, K, Li, Ag), can effectively enhance electrical properties of KNN ceramics by constructing the multiphase boundary.[3–8,10,14–16] Therefore, these additives are good candidates for constructing phase boundary to improve the electricity (especially the piezoelectric properties) in KNN-based ceramics.

As we known, La^{3+} has properties similar to Bi^{3+}, such as the similar ionic radius, same valence state, and so on. Consequently, we exploited a new lead-free piezoelectric material system of $(1-x)K_{0.44}Na_{0.56}Nb_{0.96}Sb_{0.04}O_3$-$xBi_{0.45}La_{0.05}Na_{0.5}ZrO_3$ prepared by normal sintering, and systemically investigated both their electrical performance and temperature stability. Through optimizing the composition, and the R–O–T phase boundary was mediated in this ceramics. The relatively good comprehensive performance (*e.g.*, $d_{33} \sim 455 \pm 10$ pC N^{-1}, $k_p \sim 0.47 \pm 0.02$, $T_C \sim 266$ °C, strain ∼ 0.148%, and $d_{33}^* \sim 493$ pm V^{-1}) is obtained in the ceramics with $x = 0.040$, which is attributed to the construction of R–O–T phase boundary. Moreover, a good temperature stability of remnant polarization (P_r) as well as strain value ($P_{r100\ °C}/P_{rRT} \sim 89.6\%$, $P_{r180\ °C}/P_{rRT} \sim 73.2\%$, $S_{100\ °C}/S_{RT} \sim 92.6\%$, $S_{180\ °C}/S_{RT} \sim 74.1\%$) is gained in KNNS-0.040BLNZ ceramics with a broad temperature range from room temperature to 180 °C. The related physical mechanisms were addressed.

---

[a] *Physics Department, Sichuan Province Key Laboratory of Information Materials, Southwest Minzu University, Chengdu 610041, P. R. China. E-mail: majian33@hotmail.com*

[b] *Sichuan Province Key Laboratory of Information Materials and Devices Application, Chengdu University of Information Technology, Chengdu 610225, P. R. China. E-mail: wubo7788@126.com*

2. Experimental procedure

$(1-x)K_{0.44}Na_{0.56}Nb_{0.96}Sb_{0.04}O_3$-$xBi_{0.45}La_{0.05}Na_{0.5}ZrO_3$ ($0 \leq x \leq 0.06$) piezoelectric ceramics were prepared by the conventional solid-state reaction process. Raw materials [Na_2CO_3 (99.8%), K_2CO_3 (99%), Nb_2O_5 (99.5%), Sb_2O_3 (99%), ZrO_2 (99%), Bi_2O_3 (99.999%), and La_2O_3 (99.99%)] were weighed according to chemical formula above. The powder dried and calcined at 850 °C for 6 hours after milled with ZrO_2 balls for 24 hours with alcohol as the dispersion medium, and then pressed into the pellets (~10 mm diameter, ~1 mm thickness) under a pressure of ~10 MPa when the calcined powders were mixed with ~8 wt% polyvinyl alcohol (PVA). After the PVA binder was burnt out, the samples were sintered at 1110–1130 °C for 3 hours in air, and then printed with silver paste on the both sides as the electrode. All specimens were polarized in a silicone oil bath at room temperature under a dc field of 3 kV mm^{-1} for 30 min.

The phase structure of the sintered cylindrical pellets is identified by X-ray diffraction meter (Cu_α, DX-2700, Dandong, China), measured at 40 kV and 30 mA. The field-emission scanning electron microscope (FE-SEM) (JSM-7500, Japan) has been used to measure their surface micro-structure and chemical compositions. The dielectric properties of the sintered samples were measured using an LCR analyzer (HP 4980, Agilent, U.S.A.) with varied temperatures in the range of −150–200 °C and 25–450 °C. The P–E loops and S–E curves of the cylindrical pellets were investigated by the ferroelectric tester (aixACCT, TF Analyzer 2000E, Germany). The k_p was measured by a resonance-antiresonance method with the impedance analyzer (Impedance Analyzer, PV70A, Beijing, China). The d_{33} was measured by the commercial Berlincourt-type of d_{33} meter, (ZJ-3A, China) for the poled samples.

3. Results and discussion

The XRD patterns of the KNNS-xBLNZ ($0 \leq x \leq 0.06$) ceramics in the 2θ range of 20–60° is shown in Fig. 1(a). All samples exhibit a pure perovskite structure, indicating that BLNZ has completely diffused into the KNNS lattice to form a solid solution. The O phase is characterized by (220)/(020) peaks splitting at about 45°, that is, the intensity ratio (2 : 1) between the left peak and the right one means the O symmetry.[22,23] From the Fig. 1(b), we can find that an O phase was formed in the ceramics ($0 \leq x < 0.020$), and other ceramics ($0.02 \leq x < 0.060$) demonstrate multiphase structure. To further explore their phase structure of the ceramics, the ε_r–T curves (−150–200 °C) tested at 10 kHz have been plotted in Fig. 2(a)–(h). There are two obvious abnormal dielectric peaks in the ceramics with $x \leq 0.040$, which respectively correspond to their T_{R-O} at low temperature and T_{O-T} at high temperature, as is shown in Fig. 2(a)–(e).[21] The T_{O-T} (~136 °C) and T_{R-O} (~2 °C) is far to room temperature in the ceramics with $0 \leq x < 0.020$, showing that the O phase was observed [see Fig. 2(a)]. For the ceramics with $0.02 \leq x \leq 0.030$, the T_{O-T} (~87 → 75 °C) is close to room temperature and T_{R-O} (~3 → 7 °C) is below room temperature, confirming that the O–T phase was obtained [see Fig. 2(b) and (c)]. As for BLNZ content increasing from 0.035 to 0.040, T_{R-O} (~9 → 13 °C) and T_{O-T} (~51 → 40 °C) are close to room temperature, suggesting that the R–O–T phase was constructed in the ceramics [see Fig. 2(d) and (e)]. Subsequently, only one abnormal dielectric peak was observed in the ceramics with $0.045 \leq x < 0.060$, indicating that both T_{R-O} and T_{O-T} were shifted to the same temperature, and formed the R–T phase boundary [see Fig. 2(f) and (g)]. In addition, the ε_r–T curve of $x = 0.060$ becomes flat to some degree, leading to the R phase boundary [see Fig. 2(h)], which can be explained by the fined-grain [see Fig. 4(d)]. Eventually, through systematical analysis of the phase structure by XRD and ε_r–T curves, we concluded that: the ceramics with $0 \leq x < 0.020$ are an O symmetry, the ceramics with $0.020 \leq x \leq 0.030$ belong to be O–T phase coexistence, the ceramics with $0.035 \leq x \leq 0.040$ have R–O–T phase boundary, the ceramics with $0.040 < x < 0.060$ are R–T phase boundary, the ceramic with $x = 0.060$ is R phase boundary.

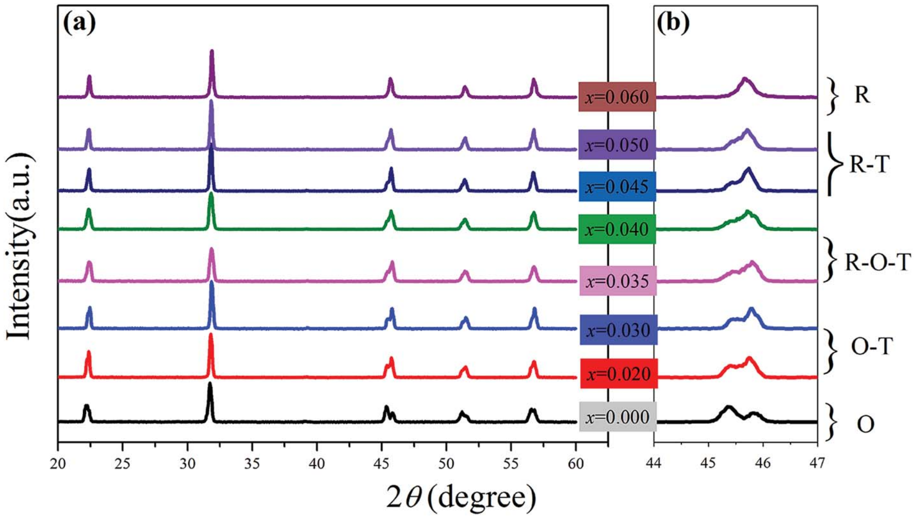

Fig. 1 XRD patterns of the $(1-x)K_{0.44}Na_{0.56}Nb_{0.96}Sb_{0.04}O_3$-$xBi_{0.45}La_{0.05}Na_{0.5}ZrO_3$ ceramics in the 2θ range of (a) 20–60°, (b) 44–47°.

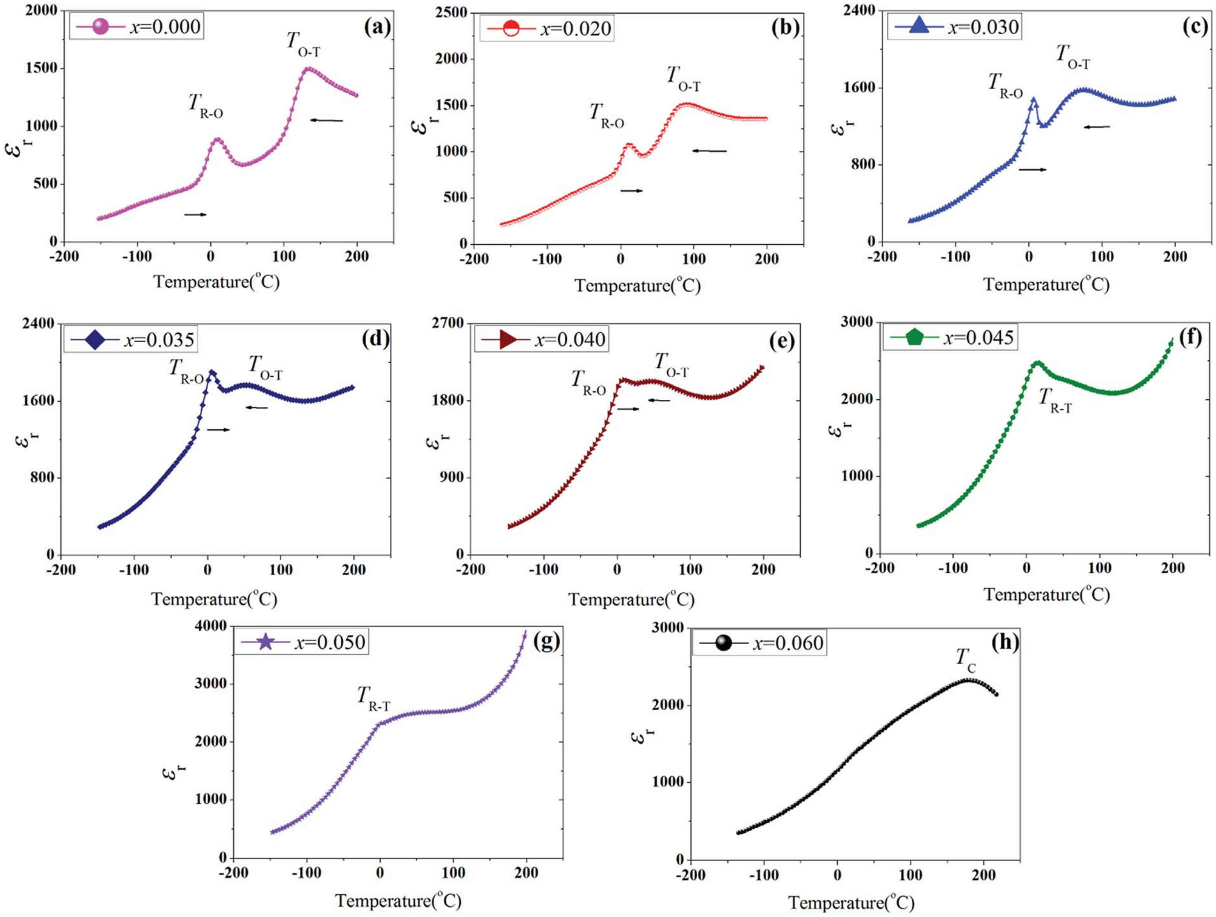

Fig. 2 ε_r–T curves of $(1-x)K_{0.44}Na_{0.56}Nb_{0.96}Sb_{0.04}O_3$-$x$$Bi_{0.45}La_{0.05}Na_{0.5}ZrO_3$ ceramics in temperature range of −150–200 °C.

Fig. 3(a) shows the ε_r–T curves (∼25–450 °C) of the KNNS-xBLNZ ceramics. We have concentrated mainly on the variation of ferroelectric–paraelectric phase transition temperature (T_C) *versus* BLNZ content. One can see that the T_C decreases with increasing the BLNZ content. Fig. 3(b) plots the corresponding phase diagrams of the ceramics as a function of BLNZ content. One can see that the T_C and T_{O-T} values have a similar variation trend, that is, they reduce monotonously with increasing BLNZ content, but the T_{R-O} rises. It is reported that both $(Bi_{0.45}La_{0.05}Na_{0.5})^{2+}$ and Zr^{4+} can simultaneously drop T_{O-T} and raise T_{R-O} in KNN-based ceramics.[3,20] Finally, the O symmetry gradually disappears with increasing of the BLNZ content, resulting in the appearance of multiphase coexistence (O–T for $0.020 \le x \le 0.030$, R–O–T for $0.035 \le x \le 0.040$, R–T for $0.040 < x < 0.060$, and R for $x = 0.060$).

Fig. 4 shows the FE-SEM micrographs of the KNNS-xBLNZ ceramics. One can see that the grain size strongly depends on the BLNZ content in this ceramics. From Fig. 4(a), a relatively

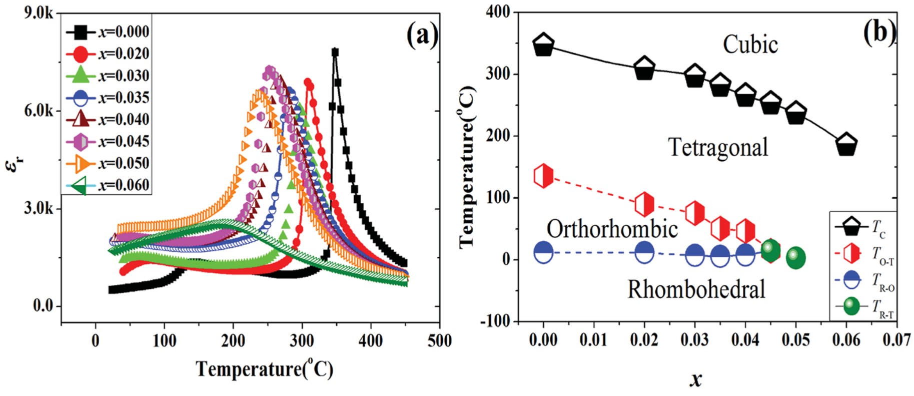

Fig. 3 (a)ε_r–T curves of $(1-x)K_{0.44}Na_{0.56}Nb_{0.96}Sb_{0.04}O_3$-$x$$Bi_{0.45}La_{0.05}Na_{0.5}ZrO_3$ ceramics in temperature range of 20–450 °C; (b) Phase diagrams of $(1-x)K_{0.44}Na_{0.56}Nb_{0.96}Sb_{0.04}O_3$-$x$$Bi_{0.45}La_{0.05}Na_{0.5}ZrO_3$ ceramics.

homogeneous grain size distribution is found in the ceramics with $x = 0$. The grain size of the ceramics ($0.020 \leq x \leq 0.040$) is increasing with introducing BLNZ content, and the inhomogeneous grains appear in the ceramics [see Fig. 4(b) and (c)]. It may be caused by the addition of Bi^{3+}, which can improve the migration rate of the grain boundary, so as to accelerate the grain growth of the KNN-based ceramics due to the formation of liquid phase.[25] Moreover, the small grains stuff the aperture of the large ones can lead to the formation of the dense microstructure in the ceramics. One can find that the grain size sharply decreases as BLNZ content increases to 0.060 [see Fig. 4(d)], which can be interpreted as the inhibited grain growth due to the aggregation at grain boundaries of both excessive Zr^{4+} and Bi^{3+}.[24,25] In addition, the fine-grain plays a key role in the flat dielectric peak in the ceramics of $x = 0.060$. The element mapping (K, Na, Nb, Sb, Bi, La, Zr, O) of KNNS-*x*BLNZ ceramics with $x = 0.040$ is shown in Fig. 5 shows. All chemical elements in the ceramics distribute uniformity.

Fig. 6 shows ε_r and tan δ values of KNNS-*x*BLNZ ceramics. One can find that the ε_r value is sensitive to the BLNZ content, that is, ε_r value rises sharply with increasing BLNZ content, getting a high value (2003–2376) in the ceramics with $0.035 \leq x \leq 0.050$, which can be ascribed to the existence of multiphase boundary. The tan δ value almost fluctuates in the range of 0.035–0.044 in the ceramics due to the dense microstructure, as is shown in Fig. 6.

Fig. 7(a) plots the *P*–*E* loops of KNNS-*x*BLNZ ceramics. We can see that all ceramics exhibit typical ferroelectric loops in Fig. 7(a). The remnant polarization (P_r) and the coercive field (E_c) as a function of BLNZ content were shown in Fig. 7(b). As is known, the P_r value is the remained aligned dipoles after removing electric field, and the E_c value is the electric field required for domain switching. The P_r value slowly decreases with increasing BLNZ content to 0.045, and then reduces sharply with further increasing the BLNZ content [see Fig. 7(b)]. The E_c value almost fluctuates in the range of 7.8–9.5 kV cm^{-1} in the ceramics [See Fig. 7(b)]. The piezoelectric properties of KNNS-*x*BLNZ ceramics is plotted in Fig. 8(a). One can see that the d_{33} value firstly increases and then decreases as increasing the BLNZ content. The k_p value firstly keeps stable with increasing the BLNZ content to 0.045, and then decreases sharply with further increasing the BLNZ content. Owing to the coexistence multiphase of R–O–T, an optimum piezoelectric ($d_{33} \sim 455 \pm 10$ pC N^{-1}, $k_p \sim 0.47 \pm 0.02$) properties were obtained in the ceramics with $x = 0.040$. It can be explained by the following two aspects: firstly, the multiphase boundaries have more equivalent spontaneous polarization vectors, indicating that it can provide more polarization vectors than the one with a pure phase structure. Secondly, the polarization anisotropic energy of the ceramics can be decreased in multiphase coexistence, which provides a shortcut for polarization rotation in anisotropically flattened free energy profile.[26–28] As is known, the formula of $d_{33} \sim \alpha\varepsilon_r P_r$ appears to be well established in KNN-based ceramics,[29,30] namely, the higher d_{33} value should be closely correlated with the higher $\varepsilon_r P_r$ value in the ceramics. To explore the relationship between d_{33} and $\varepsilon_r P_r$, a diagram of d_{33} and $\varepsilon_r P_r$ *vs.* BLNZ content is shown in Fig. 8(b). One can see that there is a similar trend for the d_{33} and $\varepsilon_r P_r$ *vs.* BLNZ content. Therefore, the improvement of piezoelectric properties can be ascribed to the multiphase coexistence, dielectric and ferroelectric properties.

Bipolar electric field induced strain curves of KNNS-*x*BLNZ ceramics is shown in Fig. 9(a). A typical butterfly shape strain

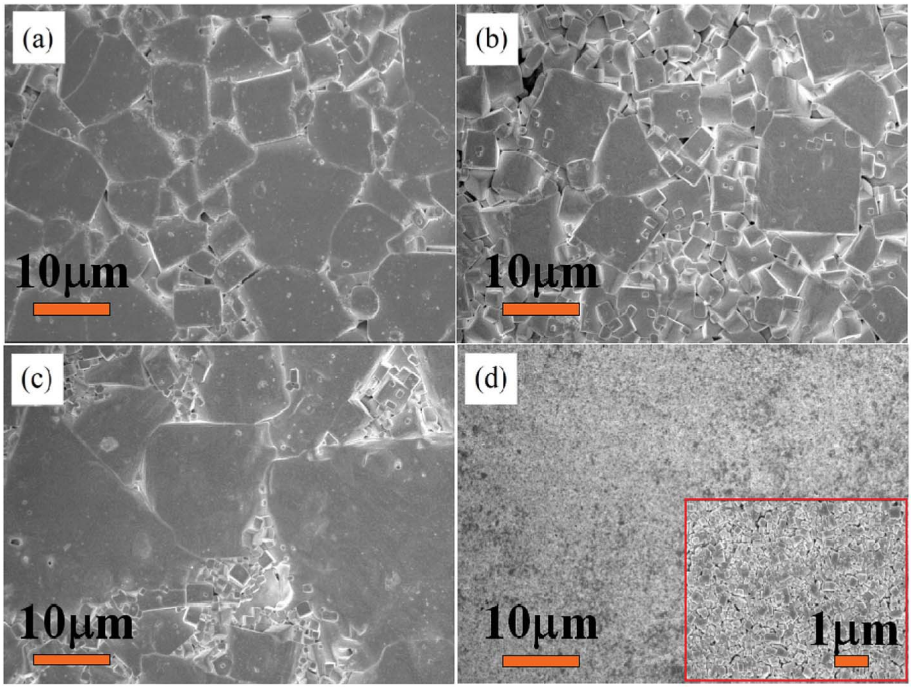

Fig. 4 FE-SEM surface images of $(1 - x)K_{0.44}Na_{0.56}Nb_{0.96}Sb_{0.04}O_3$-$x$$Bi_{0.45}La_{0.05}Na_{0.5}ZrO_3$ ceramics with (a) $x = 0$, (b) $x = 0.020$, (c) $x = 0.040$, (d) $x = 0.060$.

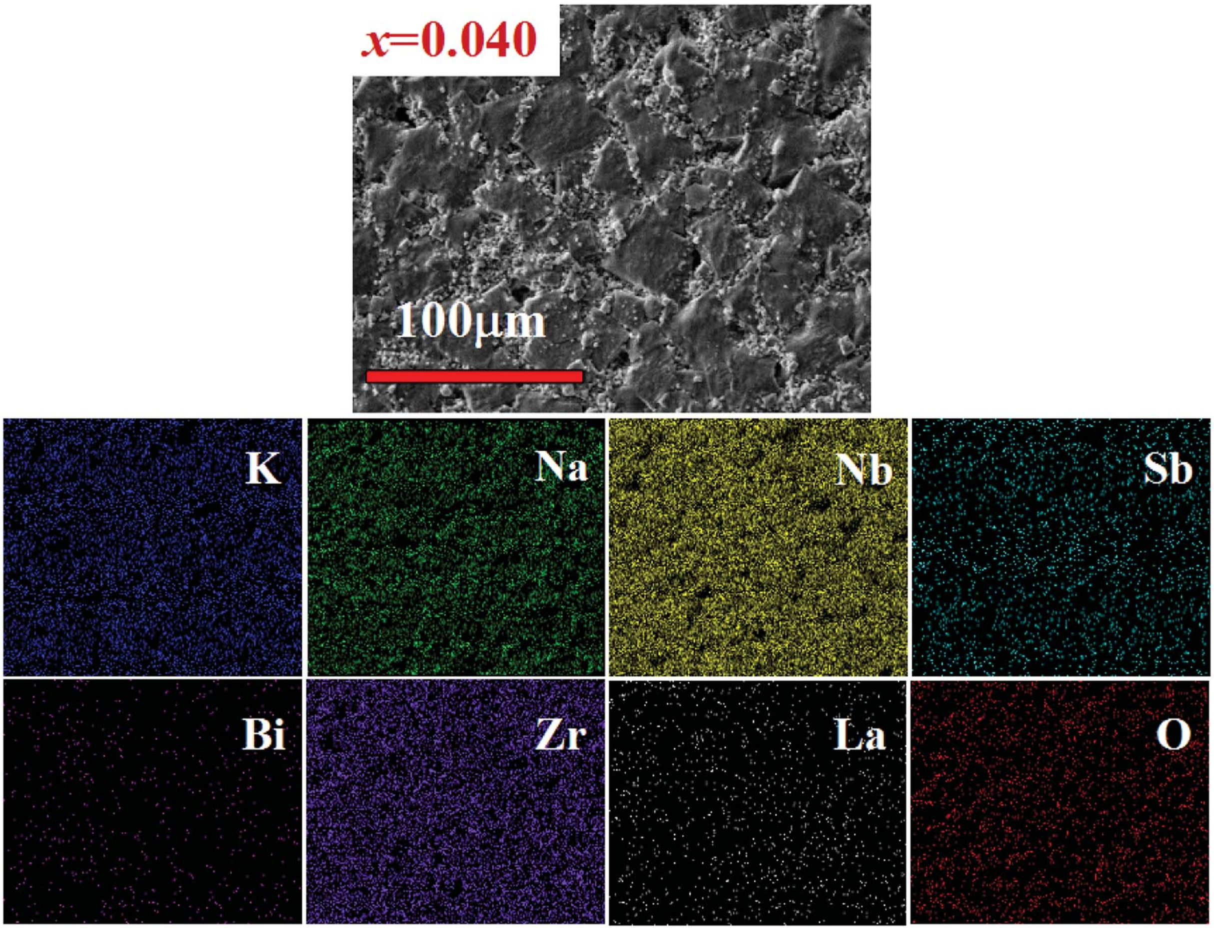

Fig. 5 Elemental (K, Na, Nb, Sb, Bi, La, Zr, and O) mapping on the surface of $(1-x)K_{0.44}Na_{0.56}Nb_{0.96}Sb_{0.04}O_3$-$xBi_{0.45}La_{0.05}Na_{0.5}ZrO_3$ ceramics with $x = 0.040$.

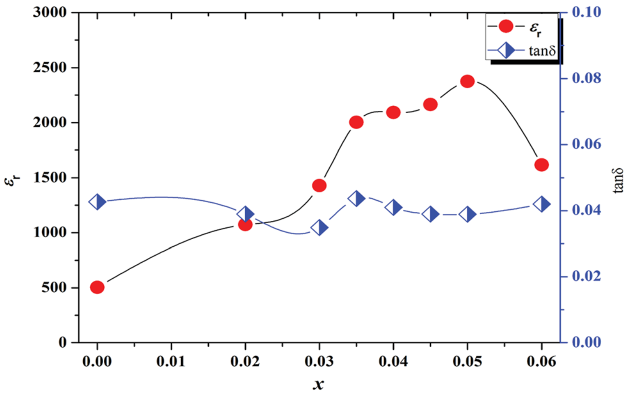

Fig. 6 Dielectric (ε_r, tan δ) properties of $(1-x)K_{0.44}Na_{0.56}Nb_{0.96}$-$Sb_{0.04}O_3$-$xBi_{0.45}La_{0.05}Na_{0.5}ZrO_3$ ceramics.

curves as a characteristic of the ferroelectric is exhibited in all ceramics. It was reported that the electric field-induced strain comes from intrinsic and extrinsic contributions. The intrinsic contributions mainly include the piezoelectric effects and electrostriction, and the extrinsic contributions are attributed to domain wall movement. In addition, the perfectly linear *S*–*E* response is the main contribution by the piezoelectric effect is, and the domain switching mainly produce "butterfly shape" of *S*–*E* loops.[31] In this work, one can see that the "butterfly shape" of *S*–*E* loops is obtained in ceramics with $0 \leq x \leq 0.050$. It can be explained by the intrinsic effect which is aligned with the lattice response and the extrinsic effect which is aligned with domain switching; Moreover, the nearly linear response of strain is observed in the ceramics with $x = 0.060$, indicating that both the lattice response and domain wall movement contribute to the strain. Fig. 9(b) shows the strain and d_{33}^* values *vs.* the compositions of BLNZ. The strain and d_{33}^* value is similar variation with increasing BLNZ content, that is, the strain value firstly increases, and then decreases with increasing the BLNZ, obtaining the maximum value (strain ~ 0.148%, $d_{33}^* \sim 493$ pm V^{-1}) at $x = 0.040$, which is benefit from the multiphase zone.

Fig. 10(a) represents the temperature-dependent *P*–*E* curves of the ceramics with $x = 0.040$, measured at $f = 1$ Hz and room temperature to 180 °C. One can find that all are statured *P*–*E* loops with increasing the measured temperature. The remnant polarization P_r changed slightly with high P_{rT}/P_{rRT} (P_{rT} is the P_r value which measured at the temperature of *T*; P_{rRT} is the P_r value which measured at room temperature) values ($P_{r100\ °C}/P_{rRT} \sim 89.6\%$, $P_{r180\ °C}/P_{rRT} \sim 73.2\%$) in the wide temperature range

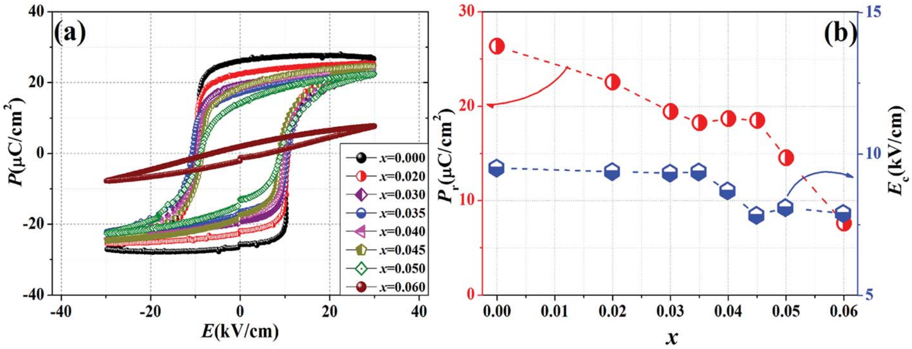

Fig. 7 Ferroelectric loops of $(1-x)K_{0.44}Na_{0.56}Nb_{0.96}Sb_{0.04}O_3$-$xBi_{0.45}La_{0.05}Na_{0.5}ZrO_3$ ceramics.

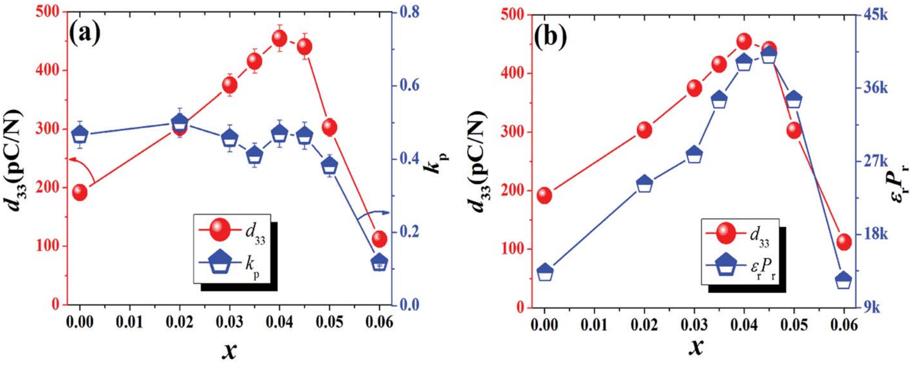

Fig. 8 (a) Piezoelectric (d_{33}, k_p) properties of $(1-x)K_{0.44}Na_{0.56}Nb_{0.96}Sb_{0.04}O_3$-$xBi_{0.45}La_{0.05}Na_{0.5}ZrO_3$ ceramics; (b) d_{33} and ε_rP_r properties of $(1-x)K_{0.44}Na_{0.56}Nb_{0.96}Sb_{0.04}O_3$-$xBi_{0.45}La_{0.05}Na_{0.5}ZrO_3$ ceramics.

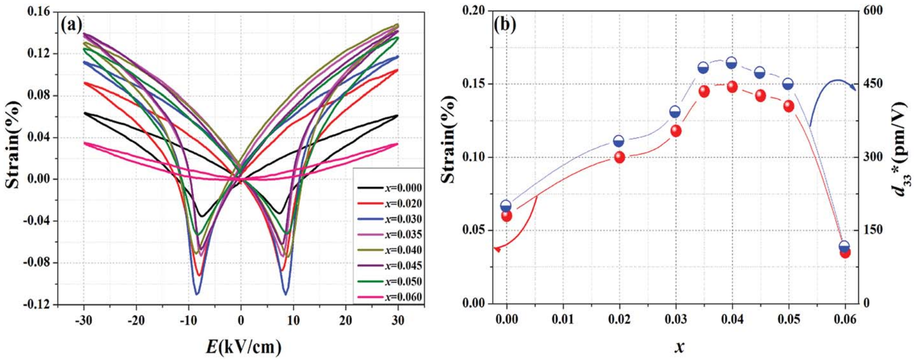

Fig. 9 Bipolar electric field induced strain of $(1-x)K_{0.44}Na_{0.56}Nb_{0.96}Sb_{0.04}O_3$-$xBi_{0.45}La_{0.05}Na_{0.5}ZrO_3$ ceramics.

[see Fig. 10(b) and (c)]. It indicates that the switched polarization state along the direction of the external electric field was of little variation. As another important characteristic for ferroelectric property, the coercive field (E_c) which indicates the energy barrier between the equivalent states of the order parameter decreased on increasing temperature. Fig. 10(d) shows bipolar electric field induced strain curves *vs.* temperature of KNNS-*x*BLNZ ceramics, measured at room temperature to 180 °C. All the strain curves show the typical butterfly shape. Different from the hysteresis loops, which involved all domain switching, the bipolar strain curves only reflected the population of non-180° domain switching. For ferroelectrics, the non-180° polarization switching is always coupled to the lattice strain, an instability in polarization orientation (*i.e.*, isotropy of polarization) will necessarily induce a softening in elastic modulus, and hence a high electrostrain. Therefore, low polarization anisotropy and elastic softening go hands in hands with each other, both contributing to a high electrostrain. As summarized in Fig. 10(b), the S_{neg} (the strain between minimum strain and strain under zero electric field) of the ceramics decreased. The changes in S_{neg} can be explained by the quantity of 90°/180° domain increased and tetragonality c/a decreased with increasing temperature approaching its T_C. While the S_{pos} (the strain between the maximum strain and the

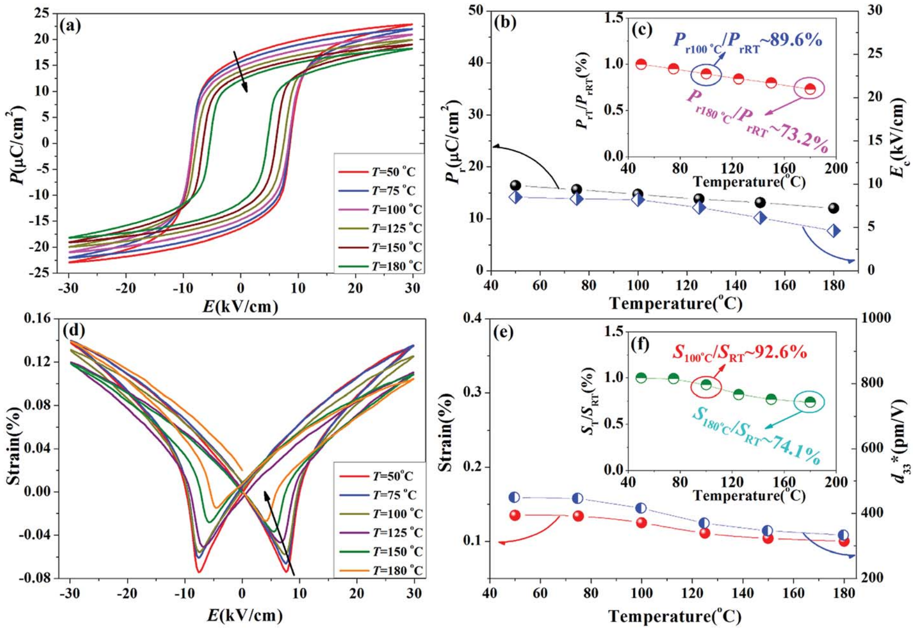

Fig. 10 Ferroelectric loops and bipolar electric field induced strain of $0.96K_{0.44}Na_{0.56}Nb_{0.96}Sb_{0.04}O_3$-$0.04Bi_{0.45}La_{0.05}Na_{0.5}ZrO_3$ ceramics as a function of temperature from room temperature to 180 °C.

strain under zero electric field) showed little change with high S_T/S_{RT} (S_T is the S value which measured at the temperature of T; S_{RT} is the S value which measured at room temperature) values ($S_{100\ °C}/S_{RT} \sim 92.6\%$, $S_{180\ °C}/S_{RT} \sim 74.1\%$) in the wide temperature range [see Fig. 10(e) and (f)]. The excellent temperature stability is due to the high T_C (~266 °C) and relatively stable ε_r in this composition, which has been demonstrated elsewhere.[35] Therefore, the P_r and strain values of KNNS-xBLNZ ceramics with $x = 0.040$ exhibit excellent temperature stability ($P_{r100\ °C}/P_{rRT} \sim 89.6\%$, $P_{r180\ °C}/P_{rRT} \sim 73.2\%$, $S_{100\ °C}/S_{RT} \sim 92.6\%$, $S_{180\ °C}/S_{RT} \sim 74.1\%$) in the wide temperature range.

4. Conclusion

$(1-x)K_{0.44}Na_{0.56}Nb_{0.96}Sb_{0.04}O_3$-$xBi_{0.45}La_{0.05}Na_{0.5}ZrO_3$ lead-free ceramics were developed by the normal sintering, and the effects of BLNZ content on their phase structure and electrical properties was investigated. The R–O–T coexistence phase has been confirmed by both XRD patterns and ε_r–T curves in the ceramics with $0.035 \leq x \leq 0.040$. Through optimizing the composition, the relatively good comprehensive performance (*e.g.*, $d_{33} \sim 455 \pm 10$ pC N^{-1}, $k_p \sim 0.47 \pm 0.02$, $T_C \sim 266$ °C, strain ~ 0.148%, and $d_{33}^* \sim 493$ pm V^{-1}) is obtained in the ceramics with $x = 0.040$ which is attributed to the construction of rhombohedral–orthorhombic–tetragonal (R–O–T) phase boundary. Moreover, a good temperature stability of remnant polarization (P_r) as well as strain value ($P_{r100\ °C}/P_{rRT} \sim 89.6\%$, $P_{r180\ °C}/P_{rRT} \sim 73.2\%$, $S_{100\ °C}/S_{RT} \sim 92.6\%$, $S_{180\ °C}/S_{RT} \sim 74.1\%$) is gained in KNNS-0.040BLNZ ceramics with a broad temperature range from room temperature to 180 °C. Hence, such a material is promising for practical applications in the piezoelectric material markets.

Conflicts of interest

There are no conflicts to declare.

Acknowledgements

Authors gratefully acknowledge the support of the National Science Foundation of China (Grant No. 51702028), and Scientific Research Project of Sichuan Provincial Department of Education (Grant No. 2018Z115).

References

1 B. Jaffe, W. R. Cook and H. Jaffe, *Piezoelectric Ceramics*, Academic, New York, 1971.

2 Y. Saito, H. Takao, T. Tani, T. Nonoyama, K. Takatori, T. Homma, T. Nagaya and M. Nakamura, *Nature*, 2004, **432**, 84–87.

3 J. G. Wu, D. Q. Xiao and J. G. Zhu, *Chem. Rev.*, 2015, **115**, 2559–2595.

4 K. Xu, J. Li, X. Lv, J. G. Wu, X. X. Zhang, D. Q. Xiao and J. G. Zhu, *Adv. Mater.*, 2016, **28**(38), 8519–8523.

5 B. Wu, H. J. Wu, J. G. Wu, D. Q. Xiao, J. G. Zhu and S. J. Pennycook, *J. Am. Chem. Soc.*, 2016, **138**, 15459–15464.

6 X. P. Wang, J. G. Wu, D. Q. Xiao, J. G. Zhu, X. J. Cheng, T. Zheng, B. Y. Zhang, X. J. Lou and X. J. Wang, Giant piezoelectricity in potassium–sodium niobate lead-free ceramics, *J. Am. Chem. Soc.*, 2014, **136**, 2905–2910.

7 T. Zheng, H. J. Wu, Y. Yuan, X. Lv, Q. Li, T. Men, C. L. Zhao, D. Q. Xiao, J. G. Wu, K. Wang, J. F. Li, Y. L. Gu, J. G. Zhu and S. J. Pennycook, *Energy Environ. Sci.*, 2017, **10**(2), 528–537.

8 B. Wu, J. G. Wu, D. Q. Xiao and J. G. Zhu, *Dalton Trans.*, 2015, **44**(48), 21141–21152.

9 K. Wang and J. F. Li, *Appl. Phys. Lett.*, 2007, **91**, 262902.

10 T. Zheng, J. G. Wu, X. J. Cheng, X. P. Wang, B. Y. Zhang, D. Q. Xiao, J. G. Zhu, X. J. Lou and X. J. Wang, *Dalton Trans.*, 2014, **43**(30), 11759–11766.

11 Y. Guo, K. I. Kakimoto and H. Ohsato, *Mater. Lett.*, 2005, **59**, 241–244.

12 M. H. Zhang, K. Wang, Y. J. Du, G. Dai, W. Sun, G. Li, D. Hu, H. C. Thong, C. L. Zhao, X. Q. Xi, Z. X. Yue and J. F. Li, *J. Am. Chem. Soc.*, 2017, **139**(10), 3889–3895.

13 P. Zhao and B. P. Zhang, *J. Am. Ceram. Soc.*, 2008, **91**, 3078–3081.

14 Z. Wang, D. Q. Xiao, J. G. Wu, M. Xiao, F. X. Li and J. G. Zhu, *J. Am. Ceram. Soc.*, 2014, **97**(3), 688–690.

15 T. Zheng, Y. Zu and J. Wu, *J. Alloys Compd.*, 2015, **647**, 927–934.

16 X. P. Wang, J. G. Wu, X. Lv, H. Tao, X. J. Cheng, T. Zheng, B. Y. Zhang, D. Q. Xiao and J. G. Zhu, *J. Mater. Sci.: Mater. Electron.*, 2014, **25**, 3219–3225.

17 F. Z. Yao, K. Wang, W. Jo, Y. G. Webber, T. P. Comyn, J. X. Ding, B. Xu, L. Q. Cheng, M. P. Zheng, Y. D. Hou and J. F. Li, *Adv. Funct. Mater.*, 2016, **26**, 1217–1224.

18 F. Z. Yao, Q. Yu, K. Wang, Q. Li and J. F. Li, *RSC Adv.*, 2014, **4**, 20062–20068.

19 T. Zheng, J. G. Wu, X. J. Cheng, X. P. Wang, B. Y. Zhang, D. Q. Xiao, J. G. Zhu and X. J. Lou, *Dalton Trans.*, 2014, **43**(25), 9419–9426.

20 B. Chen, J. Ma, S. Wu and B. Wu, *J. Mater. Sci.: Mater. Electron.*, 2017, **28**, 3299–3308.

21 B. Wu, J. Ma, W. J. Wu, M. Chen and Y. C. Ding, *Ceram. Int.*, 2018, **44**(1), 1172–1175.

22 K. Wang and J. F. Li, *Appl. Phys. Lett.*, 2007, **91**, 262902.

23 H. Du, W. Zhou, F. Luo, D. Zhu, S. Qu, Y. Li and Z. Pei, *J. Appl. Phys.*, 2008, **104**(3), 034104.

24 B. Malic, J. Bernard, A. Bencan and M. Kosec, *J. Eur. Ceram. Soc.*, 2008, **28**, 1191–1196.

25 J. Noh and J. Yoo, *J. Electroceram.*, 2012, **29**(2), 144–148.

26 J. H. Gao, L. X. Zhang, D. Z. Xue, T. Kimoto, M. H. Song, L. S. Zhong and X. B. Ren, *J. Appl. Phys.*, 2014, **115**, 054108.

27 D. S. Keeble, E. R. Barney, D. A. Keen, M. G. Tucker, J. Kreisel and P. A. Thomas, *Adv. Funct. Mater.*, 2013, **23**, 185–190.

28 W. H. Ma and A. Hao, *J. Appl. Phys.*, 2014, **115**, 104105.

29 J. Li, F. Li and S. J. Zhang, *J. Am. Ceram. Soc.*, 2014, **97**, 1–27.

30 F. Rubio-Marcos, R. López-Juárez, R. E. Rojas-Hernandez, A. D. Campo, N. Razo-Pérez and J. F. Fernandez, *ACS Appl. Mater. Interfaces*, 2015, **7**, 23080–23088.

31 G. Viola, T. Saunders, X. Wei, K. B. Chong, H. Luo, M. J. Reece and H. Yan, *J. Adv. Dielectr.*, 2013, **3**, 1350007–1350011.

32 P. Li, J. Zhai, B. Shen, S. Zhang, X. Li, F. Zhu and X. Zhang, *Adv. Mater.*, 2018, **30**(8), 1705171.

33 B. Liu, P. Li, B. Shen, J. Zhai, Y. Zhang, F. Li and X. Liu, *J. Am. Ceram. Soc.*, 2018, **101**(1), 265–273.

34 B. Liu, X. Liu, P. Li, F. Li, B. Shen and J. Zhai, *RSC Adv.*, 2017, **7**(66), 41788–41795.

35 X. Lv, J. Wu, D. Xiao, J. Zhu, J. Zhang and X. X. Zhang, *Adv. Electron. Mater.*, 2018, 1800205.